

Article

Geochemical Characteristics of Mineral Assemblages from the Yamansu Iron Deposit, NW China, and Their Metallogenic Implications

Zhiyuan Sun *, Jingbin Wang, Yuwang Wang and Lingli Long

Technic Research Center for Deep Resources Exploration in Non-Ferrous Metal Mines, Beijing Institute of Geology for Mineral Resources, Beijing 100012, China; wjb@bigm.cn (J.W.); wyw@cnnm.com (Y.W.); longlingli799@163.com (L.L.)

* Correspondence: sunzhiyuan010@163.com; Tel./Fax: +86-010-8492-9514

Received: 17 November 2019; Accepted: 25 December 2019; Published: 31 December 2019



Abstract: The Yamansu deposit, which is hosted in the volcanic-sedimentary sequence of the Carboniferous Yamansu Formation in Eastern Tianshan, NW China, contains many skarns, and the orebodies occur in the ore district in stratoidal, banded or lenticular forms. Four alteration stages, namely, albite–tourmaline–apatite–Gr₁ (Stage I), K-feldspar–Gr₂ (Stage II), magnetite–chlorite–epidote (Stage III), and quartz–calcite–axinite–Gr₃ (Stage IV), are distinguished in the Yamansu deposit. The mineral geochemistry associated with each different stage is presented to provide a better understanding of the corresponding metallogenic processes. The ore-forming fluid in Stage I was derived from a magmatic–hydrothermal source and formed at high temperatures with many volatiles. This ore-forming fluid, which contained considerable metallogenic materials during the early stage, likely experienced diffusive metasomatism in a closed system with low water/rock (W/R) ratios. Mineral geochemical analyses show that the Fe content gradually increases from Stage I to Stage II, indicating that accumulated ore-forming materials were available during changes in the physicochemical conditions from a reducing environment with neutral pH to oxidizing conditions with mildly acidic pH. During the main metallogenic stage (Stage III), mineral assemblages reflect moderate- to high-temperature conditions, and the ore-forming fluid was created and destroyed periodically; the magnetite ores were deposited in a fluctuating fluid system. The multilayered orebodies, multigenerational garnets, and minerals with oscillatory zoning indicate that the ore-forming fluid may have developed periodic fluctuations, and this special multistage fluctuation of the hydrothermal fluid in the Yamansu deposit was the key factor controlling the multiple extraction, enrichment and precipitation of metallogenic materials.

Keywords: minerals; geochemistry; metallogenic process; Yamansu deposit; Eastern Tianshan

1. Introduction

The Yamansu deposit is one of the submarine volcanic-hosted iron deposits in the Aqishan–Yamansu belt of the Eastern Tianshan, Xinjiang [1–3]. Skarn minerals are strongly developed within this deposit, and the occurrences of mineral assemblages in the Yamansu deposit have been mentioned [4,5]. However, the detailed relationships between associated skarn minerals and orebodies from different stages have not been delineated, which restricts any discussion of the corresponding metallogenic processes. Although earlier studies have largely focused on the deposit geology, magnetite geochemistry, and diagenetic and metallogenic ages of the deposit, few studies have examined the skarn mineral assemblages and their important implications for the evolution of ore-forming fluids and physicochemical conditions therein. Skarn minerals, especially those that preserve complex chemical

zonation patterns and show multiple growth stages, can record the composition and evolutionary history of hydrothermal fluid systems [6–9]. Furthermore, in the application of analytical techniques, including electron microprobe analysis (EMPA) and laser ablation inductively coupled plasma mass spectrometry (LA-ICP-MS), hydrothermal alteration minerals have been successfully used as important proxies for the metallogenic environment, prospecting, and the evolution of ore-forming fluids within ore deposits [10–12].

In this paper, we present the mineralogy and petrographic features representing four metallogenic stages and the major and trace element chemical data for mineral assemblages from the Yamansu deposit. We discuss the metallogenic conditions and evolution of the ore-forming fluids within the deposit with the ultimate aim to reveal the mineralogical processes that underlie the metallogenic mechanism and to develop a superior understanding of the implications for Yamansu mineralization.

2. Regional Geology

The eastern Tianshan Orogenic Belt is located at the intersection of the Siberia, Eastern Europe, Tarim and North China Cratons, and it is an important part of the Central Asian Orogenic Belt (Figure 1a) [13–15]. From North to South, the Eastern Tianshan orogenic belt successively occupies the Bogda–Harlik tectonic belt, the Turpan–Hami basin, the Jueluotage tectonic belt, and the Central Tianshan Massif (Figure 1b). As indicated by the distribution of ore deposit types and faults, the Jueluotage tectonic belt comprises the southern margin of the Turpan–Hami basin (copper belt), the Kangguer belt (gold belt), and the Aqishan–Yamansu belt (iron-copper-silver belt) (Figure 1b) [16,17]. The Aqishan–Yamansu is one of the important subunit belts in eastern Tianshan and is well known for its iron–copper deposits that are hosted in its carboniferous submarine volcanics [1,18,19]. Typical and well-known iron deposits include the Yamansu, Hongyuntan, Kumutag, and Aqishan deposits, which have similar mineralization and present orebodies that are structurally developed into banded or lens-like forms and mostly conformable with their carboniferous volcanic-sedimentary country rocks [1,3].

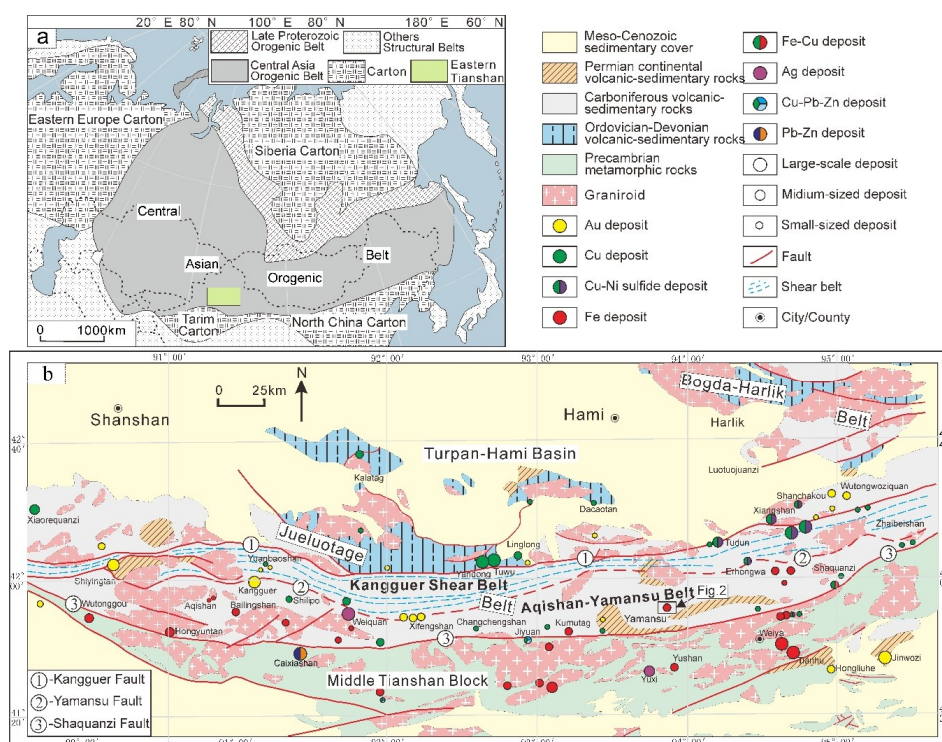


Figure 1. Tectonic sketch geological map of the Central Asian Orogenic Belt (a) and geological map with deposit distributions in the Eastern Tianshan Orogenic Belt (b), modified after [16].

3. Local Geology

3.1. Ore Deposit

The Yamansu iron deposit is located in the east-central part of the Aqishan–Yamansu belt, Xinjiang, and it was discovered by the Sixth Geological Brigade of the Xinjiang Geological and Mineral Resources Bureau in 1957. The estimated ore reserve is 3549×10^4 t with an average grade of up to 77% total Fe by the end of 2013 [20]. The main lithostratigraphic units in the Yamansu ore district are the Yamansu Formation (C_{1y}), and the Dikaner Formation (C_{2d}) strata (Figure 2). There are five carboniferous lithologies or formation units from bottom upward: (1) marble, andesite, basalt, basaltic breccia and ignimbrite intercalated with rhyolitic ignimbrite; (2) andesitic volcanic ignimbrite, andesitic pyroclastic ignimbrite and rhyolitic ignimbrite; (3) basaltic andesite and andesitic ignimbrite; (4) limestone and limestone; and (5) andesitic ignimbrite and volcanic breccia. The exposed rocks comprising the Yamansu Formation, which hosted the Yamansu orebodies, are bimodal volcanic rocks characterized by two main geochemical serie trends (calcalkaline and alkaline) with high-Na affinity [21]. The orebody-hosted volcanic rocks are mainly basalt, ignimbrite, and rhyolitic ignimbrite, which are originally derived from the parental iron-oxide melt [3,22]. The main intrusion rocks and dykes are pyroxene diorite and diabase.

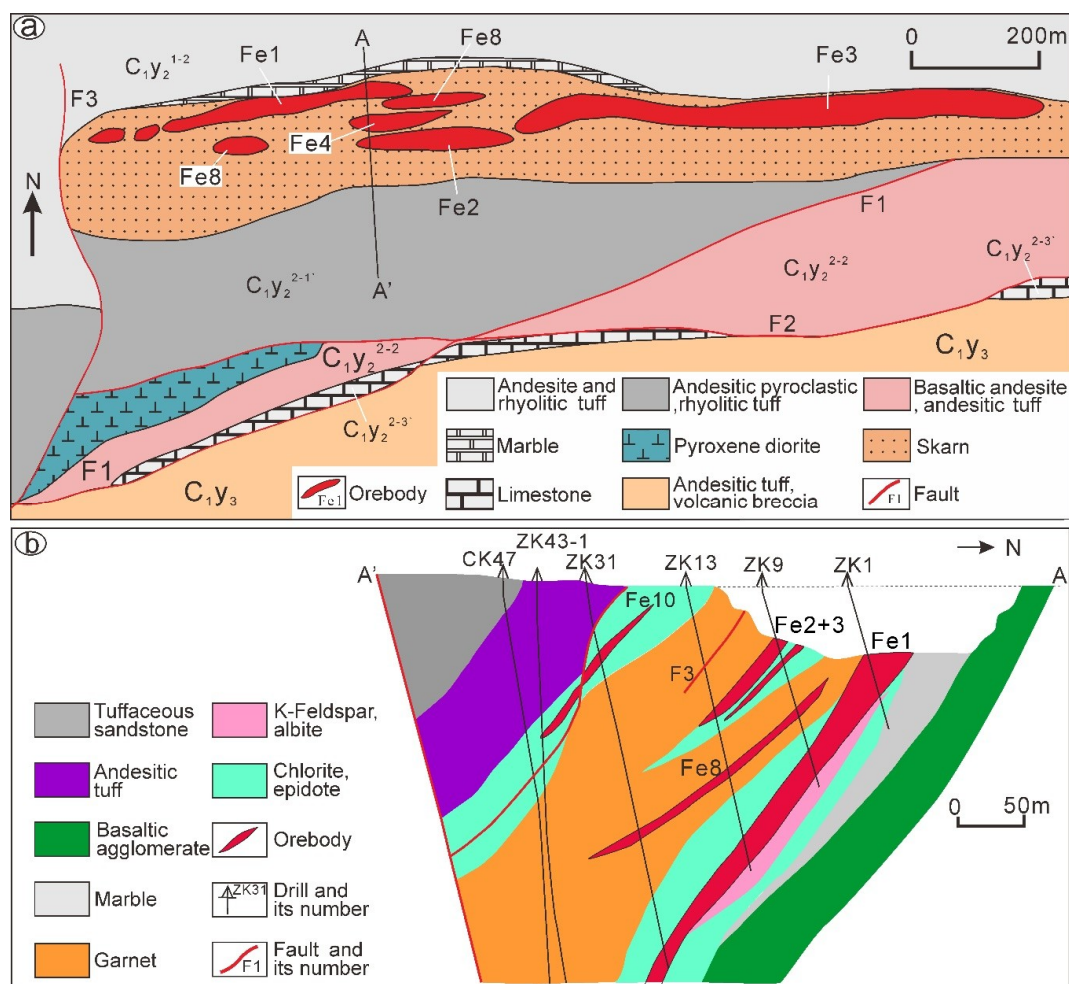


Figure 2. Geological map (a) and geological section (b) of the Yamansu iron deposit (modified from [23]).

The dominant structure is the Yamansu anticline, which has a width of 1500–2000 m, with a NE 80° trend and a dip angle of 25° [24]. The volcanic breccia and crystal ignimbrite of the Yamansu Formation constitute the core of the Yamansu anticlinorium. The skarns are extensively developed

in the deposit, and they are near EW direction with a strike length of about 1500 m and a width of 150–200 m (Figure 2a). The similar distribution of skarns and volcanic rocks and the basalts are partially replaced by andradite support the idea of a replacement of basaltic protolith into garnet skarn [25]. The orebodies of Yamansu deposit nearly occur at the axis of anticline, which nearly follow EW-direction (trend of 80°, dip angle of 60°–75°) (Figure 2b). About 16 orebodies can be recognized, with Fe1 and Fe2 + 3 being the major orebodies of the deposit. The orebodies are developed into structures with stratoidal, banded, or lenticular shapes and mostly show sharp contact with the country rocks. The orebodies are nearly parallel and display En Echelony distributions, and their maximum depth in the profile can reach 500 m (Figure 2b).

3.2. Paragenesis of Alteration

The dominant skarn minerals are garnet, chlorite, epidote, and K-feldspar with subordinate albite-plagioclase, amphibole, apatite, tourmaline, and axinite. The skarns usually show sharp contact with the orebodies. Based on the paragenesis and crosscutting relationships of the skarn minerals, we can identify four main mineralization stages (Figure 3).

The first metallogenic stage (Stage I) is represented by albite-tourmaline-apatite-garnet paragenesis. The alteration in this stage is characterized by minerals that contain volatile components (such as tourmaline) together with other accessory minerals. Isolated tourmaline and apatite from Stage I exhibit granular forms. The tourmaline crystals are characterized by large sizes, whereas apatite grains are smaller than tourmaline grains, and both are replaced by epidote and K-feldspar (Figure 4a). The mineralization of this stage consists dominantly of disseminated albite and magnetite (Figure 4b). The first-generation of garnets (Grt1) in the Stage I are brown or chocolate-brown with sizes ranging from 0.5–5 mm and are generally cut by magnetite veins (Figure 4c).

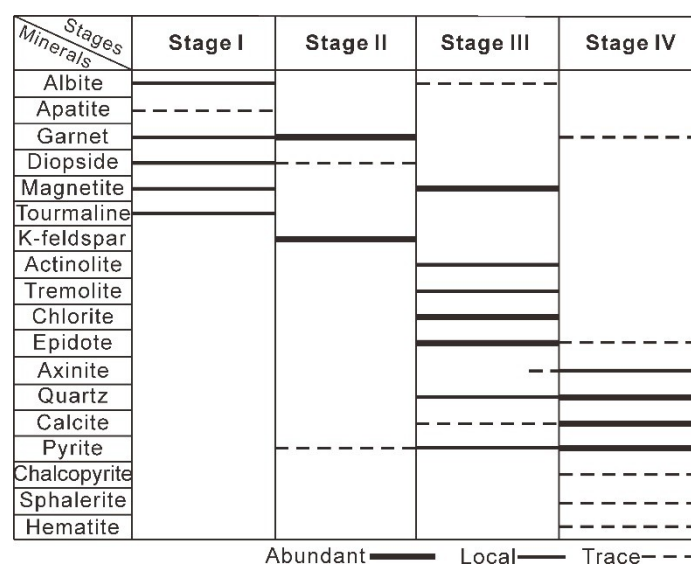


Figure 3. Alteration and mineralization paragenesis of the Yamansu iron deposit.

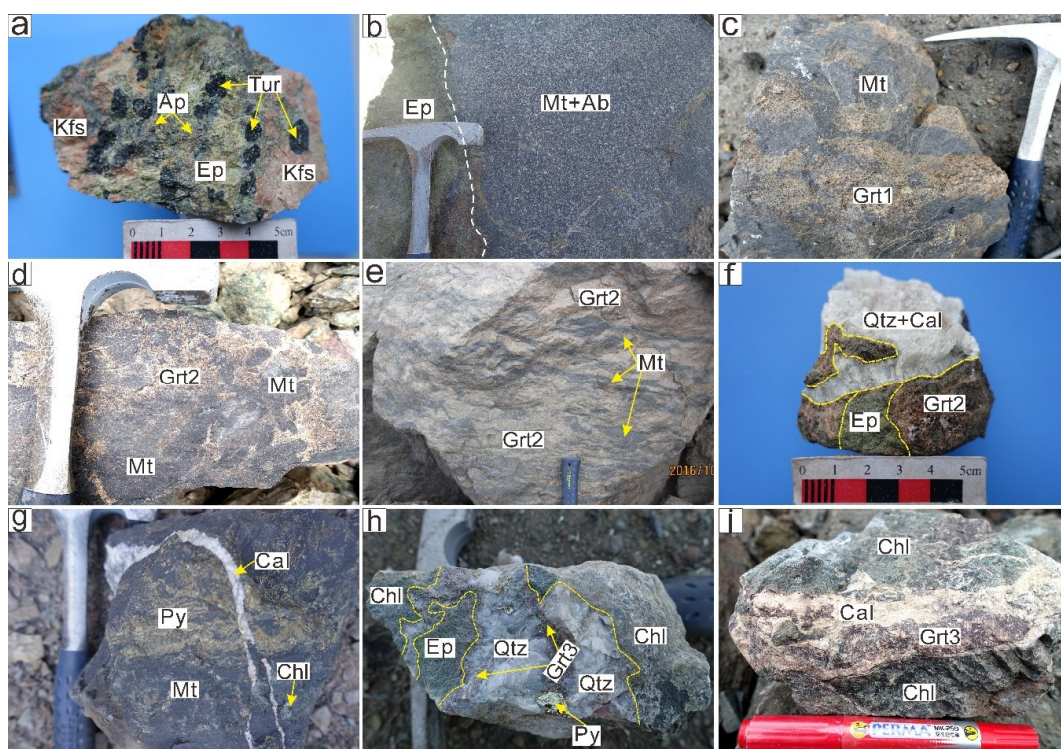


Figure 4. Photographs of representative samples and their relationships in the Yamansu deposit. (a) Granular tourmaline and apatite (fine-grained) replaced by epidote and K-feldspar; (b) Disseminated magnetite and albite replaced by epidote; (c) Massive garnet aggregates (brown or chocolate-brown, coarse-grained) cut by magnetite veins; (d,e) An intergrowth relationship with breccia and banded magnetite; (f) Garnet (Grt2) skarn cut by epidote vein and followed by quartz + calcite vein; (g) Massive magnetite + chlorite ore replaced by pyrite, and both magnetite and pyrite cut by calcite vein; (h) Chlorite + epidote skarn cut by quartz + pyrite vein (together with granular Grt3); (i) Chlorite skarn cut by calcite + Grt3 vein. Abbreviations: Tur—Tourmaline; Ap—Apatite; Ep—Epidote; Kfs—K-feldspar; Ab—Albite; Mt—Magnetite; Grt1—Garnets of the first generation; Grt2—Garnets of the second generation; Grt3—Garnets of the third generation; Qtz—Quartz; Cal—Calcite; Py—Pyrite; Chl—Chlorite.

Within the Yamansu deposit, the second metallogenic stage (Stage II) is represented by abundant K-feldspar and garnet with subordinate diopside, which occur mainly surrounding the Fe1 orebody and in the hanging wall of the Fe2 + 3 orebodies. The second-generation of garnets (Grt2) in Stage II are generally found as massive garnet aggregates or intergrown with breccia and banded magnetite (Figure 4d,e). Figure 4f shows that Grt2 is cut by epidote vein followed by quartz + calcite vein.

The third metallogenic stage (Stage III) is the major stage of iron mineralization in the Yamansu deposit. During this stage, abundant hydrothermal minerals (such as chlorite, epidote, tremolite, and actinolite) and considerable metallic minerals (mainly magnetite) formed with subordinate quartz and sulfides. The mineral parageneses are dominated by magnetite, chlorite + epidote, and magnetite + chlorite, which are mainly cut by later quartz veins or calcite veins (Figure 4g,i).

The fourth metallogenic stage (Stage IV) is characterized by abundant quartz + sulfides (mainly pyrite), quartz + calcite, quartz + axinite, and calcite + garnet (third-generation garnets, Grt3) veins with minor chalcopyrite and sphalerite. The quartz-filled fractures, which contain unusually granular Grt3 as aggregates within the quartz vein, cut the chlorite + epidote skarns (Figure 4h). In addition, calcite + Grt3 veins, which cut the chlorite skarns, also developed in Stage IV (Figure 4i).

4. Sampling and Analytical Methods

4.1. Mineral Samples

Samples for analyses with in situ EMPA (Shimadzu, Kyoto, Japan) and LA-ICP-MS (Agilent, Santa Clara, CA, USA) were collected within the Yamansu open pit. Detailed mineral samples, descriptions, and analytical items are listed in Table 1.

Table 1. The mineral samples and their characteristics from the Yamansu deposit.

Samples	Descriptions	Minerals	Analytical Items
Y6104-5	Granular tourmaline + apatite replaced by epidote	Ap, Tur	EMPA
Y6104-10	Garnet + apatite replaced by epidote and actinolite	Ap	EMPA
Y6104-11	Tourmaline + apatite replaced by epidote	Ap, Tur	EMPA
Y7729-1	Garnet + apatite crosscut by calcite veins	Ap, Grt1	EMPA
Y7729-5	Granular tourmaline aggregates	Tur	EMPA
Y7730-13	Medium-grained garnet replaced by magnetite	Grt1	EMPA, LA-ICP-MS
Y6104-4	Garnet + magnetite ore, disseminated garnet replaced by magnetite	Grt1	EMPA, LA-ICP-MS
Y5817-5	Massive garnet (medium-grained) aggregates	Grt2	EMPA
Y5818-3	Garnet + K-feldspar crosscut by quartz + pyrite vein	Grt2, Kfs	EMPA
Y7730-12	Breccia magnetite + garnet	Grt2	EMPA, LA-ICP-MS
Y6104-2	Massive magnetite + garnet	Grt2	EMPA, LA-ICP-MS
Y6104-30	Massive garnet crosscut by quartz + pyrite + garnet vein	Grt2, Grt3	EMPA
Y7801-5	Garnet + quartz + axinite vein cut chlorite skarn	Grt3	EMPA, LA-ICP-MS
Y5817-6	Garnet vein crosscut chlorite + epidote skarn	Grt3	EMPA
Y5818-2	Coarse-grained garnet sluster together with pyrite	Grt3	EMPA
Y5819-8	Garnet vein crosscut magnetite + pyrite	Grt3	EMPA
Y5818-9	Paragenesis of disseminated magnetite and granular albite	Ab	EMPA
Y5819-1	Albitized andesitic ignimbrite containing disseminated magnetite (20%)	Ab	EMPA
Y6104-14	Disseminated magnetite + albite replaced by epidote	Ab	EMPA
Y7730-8	Axinite vein cut epidote skarn	Ax	EMPA
Y7801-5	Quartz + Axinite vein crosscut chlorite skarn	Ax	EMPA

4.2. Analytical Methods

The EMPA, which includes primarily the in situ analysis of major elements and back-scattered electron (BSE) observation, was performed at the EMPA laboratory at the Institute of Geology and Geophysics of the Chinese Academy of Sciences. Before the analysis, the polished thin sections were sprayed with carbon films. The experiments were conducted using a JXA-8100 instrument, with an acceleration voltage of 15 kV, an acceleration current of 20 nA, a peak counting time of 20 s, and a beam spot diameter of 3 μm were selected as the analysis conditions. Fe_2O_3 (Fe), MnTiO_3 (Mn, Ti), diopside

(Mg, Si), Cr₂O₃ (Cr), orthoclase (Al, K), Ni (Ni), anorthite (Ca) and albite (Na) were used as standards. During the experiment, the test object was held under the secondary electron image and then selected for testing. The precision of all analyzed elements was better than 1.5%, and the lower detection limits were calculated to be on the order of 0.01 wt% for all elements. During the experiment, the test object was held under the secondary electron image and then selected for testing. Chemical formulae and end-member proportions for minerals were calculated from mineral analyses following the method of [26].

After EMPA was completed, polished thin sections of representative garnets were selected for LA-ICP-MS trace element analyses. In situ LA-ICP-MS analyses were performed at the Guangzhou Institute of Geochemistry, Chinese Academy of Sciences, using an ArF excimer laser ablation system (GeoLasPro) coupled with an Agilent 7700a ICP-MS. The details of the analytical methods are presented in [27]. Element concentrations were calibrated against multiple reference materials. United States Geological Survey (USGS) standard reference materials (SRMs) NIST-610 were used as the external standards, and ²⁹Si was used as the internal standard. ICPMSDataCal software was used to perform the offline selection and integration of the background and analysed signals, the time-drift correction and quantitative calibration for trace element analysis [27].

5. Results

5.1. Mineralogy and Petrographic Features

The tourmaline crystals from Stage I are characterized by granular textures with diameters of 0.2–5 mm and they show growth zonation (Figure 5a). In some cases, albite crystals are enclosed by tourmaline along crystal rims (Figure 5b). Apatite is also recorded to exhibit a granular texture in Stage I and is developed mainly in altered andesitic ignimbrite and tourmaline + apatite and tourmaline + garnet (Grt1) gangue minerals. Apatite crystals, which intergrown with tourmaline, show fine-grained crystals with diameters of 0.1–0.5 mm and are replaced by epidote crystals (Figure 5a). Moreover, apatite crystals intergrown with Grt1 show granular and columnar shapes (Figure 5c). The alteration and mineralization of Stage I are recorded mainly by disseminated ores. Disseminated magnetite crystals (10–200 µm in diameter) are intergrown with albite and they show euhedral to subhedral textures (Figure 5d). Replacement of magnetite by hematite is common in disseminated ores where magnetite is mostly rimmed by hematite (Figure 5d).

The Grt1 crystals in Stage I show well-preserved growth zonation. The cores of Grt1 show nearly euhedral hexagonal habitus, whereas the rims of Grt1 have large overgrowth areas under BSE observation (Figure 5e). However, the Grt2 crystals in Stage II have light yellow cores and pale or colorless rims, and Grt2 are always replaced by magnetite and quartz or cut by chlorite veins (Figure 5f). Figure 5g shows that later magnetite and quartz fill the fractures in Grt2. Occasionally, the microscopic signatures of Grt2 show irregular cores (Figure 5h), which are interpreted to indicate crystallization under nonequilibrium conditions.

As the major mineralization stage, Stage III is characterized by massive magnetite ores. The massive magnetite can be divided into two subtypes. The earlier magnetite crystals are characterized by fine euhedral habitus with growth zonation (Figure 5i), whereas the later magnetite crystals are intergrown with pyrite and are characterized by xenomorphic textures (Figure 5j). The main massive ore in Stage III consists of magnetite with a minor amount of quartz and pyrite. Microscopic features of magnetite crystals from the massive ore show granular or irregular platy textures, which are commonly replaced by quartz along their rims or fractures (Figure 5i). The axinite in the quartz + axinite vein of Stage IV is observed as euhedral wedges or rhomboidal crystals (Figure 5k). In addition, Grt3 crystals intergrown with quartz in Stage IV record thin oscillatory zoning along the rims (Figure 5l). Unlike Grt1 and Grt2 in the early stages, the Grt3 crystals in Stage IV display nearly monotonic textures and larger crystal grains >1 mm in diameter (Figure 5l).

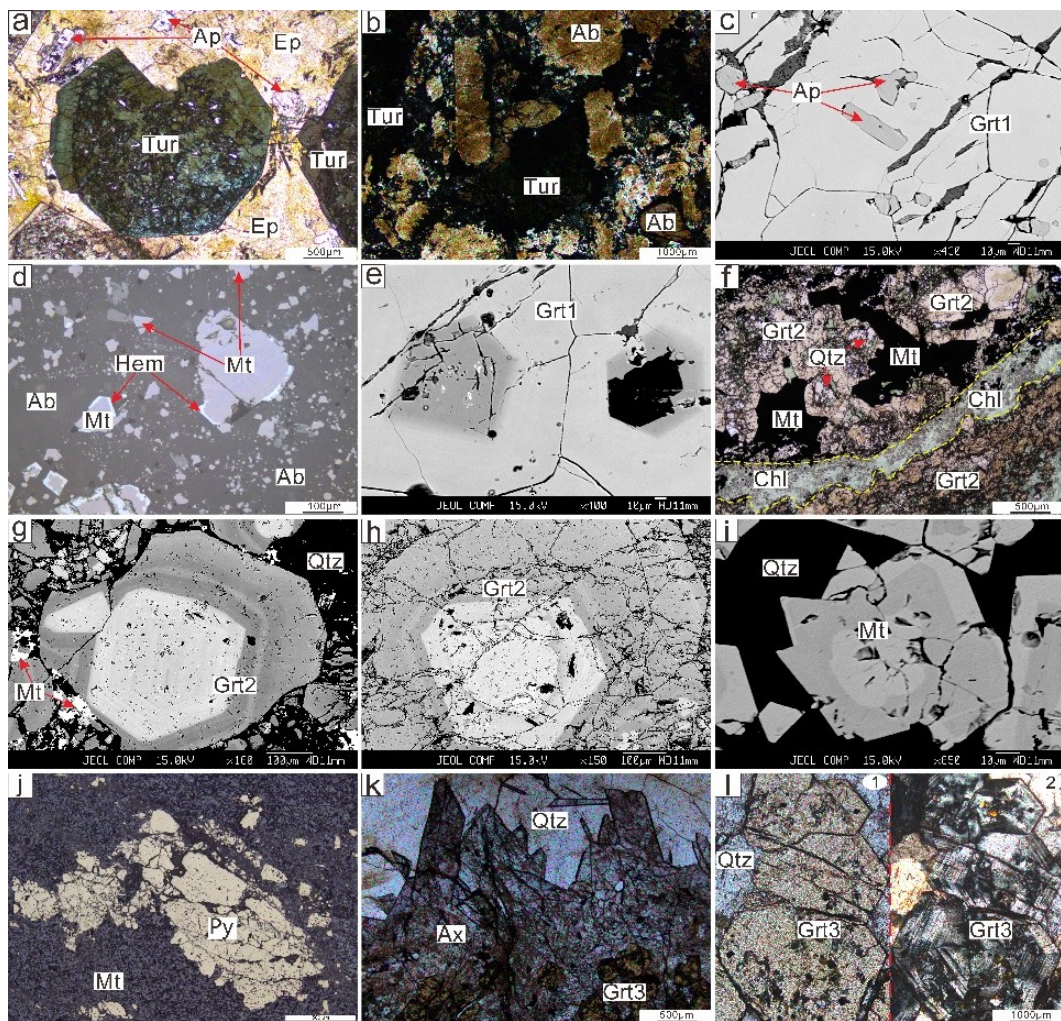


Figure 5. Photomicrographs of representative samples from different stages and their relationships in the Yamansu deposit. (a) Tourmaline (growth zonation) and apatite (fine-grained) crystals replaced by epidote (plane polarized light); (b) Albite crystals replaced or enclosed by tourmaline along their rims (cross polarized light); (c) Granular and rod-shaped apatite enclosed by Grt1 (back-scattered electron (BSE) image); (d) Disseminated euhedral to anhedral magnetite crystals with diversely 5–100 μm grains that are intergrown with albite and replaced by hematite (reflected light); (e) Grt1 characterized by core–rim growth zonation (BSE image); (f) Grt2 (with yellow cores and pale rims) show replacement by magnetite and quartz, or cut by chlorite vein (plane polarized light); (g) A Grt2 shows well-preserved growth zonation and replaced by magnetite and quartz (BSE image); (h) Euhedral Grt2 with growth zonation of irregular core (BSE image); (i) Magnetite crystals in massive ores have continuous alternate zonation with a brighter central zone and replaced by quartz (BSE image); (j) Magnetite crystals coexisting with sulfide (mainly fine to coarse grained pyrite) have xenomorphic shapes (BSE image); (k) Axinite (stumpy wedge or rhomboidal) and quartz superimposed on the Grt3 (plane polarized light); (l) Zoned Grt3 (with oscillatory zoning in the rims) accompanied with quartz (plane polarized light in 1 and cross polarized light in 2). Abbreviations: Tur—Tourmaline; Ap—Apatite; Ep—epidote; Ab—Albite; Grt1—Garnets of the first generation; Grt2—Garnets of the second generation; Grt3—Garnets of the third generation; Mt—magnetite; Hem—hematite; Qtz—quartz; Chl—chlorite; Py—pyrite; Ax—Axinite.

5.2. Major Chemical Elements of Minerals

5.2.1. Apatite

The electron microprobe data of apatite are listed in Table S1. Apatites in the Yamansu deposit generally show little compositional variation in P_2O_5 (38.84%–43.43%) and CaO (55.09%–57.52%), and have low Al_2O_3 , SiO_2 , Na_2O , and MnO contents. The calculated F contents of apatite vary between 3.06% and 3.95% and the calculated Cl contents are very low (0.05%–0.28%). Apatite crystals have high F/Cl ratios (14.29–57.59) and $F/(F+Cl)$ (X_F) values (0.93–0.99), which classify as fluor-apatites and formed at high temperature condition [28]. All the apatite crystals from the Yamansu deposit plot on the F-rich field, which is similar to that of Kiruna deposits, in the F-Cl-OH ternary diagram (Figure 6).

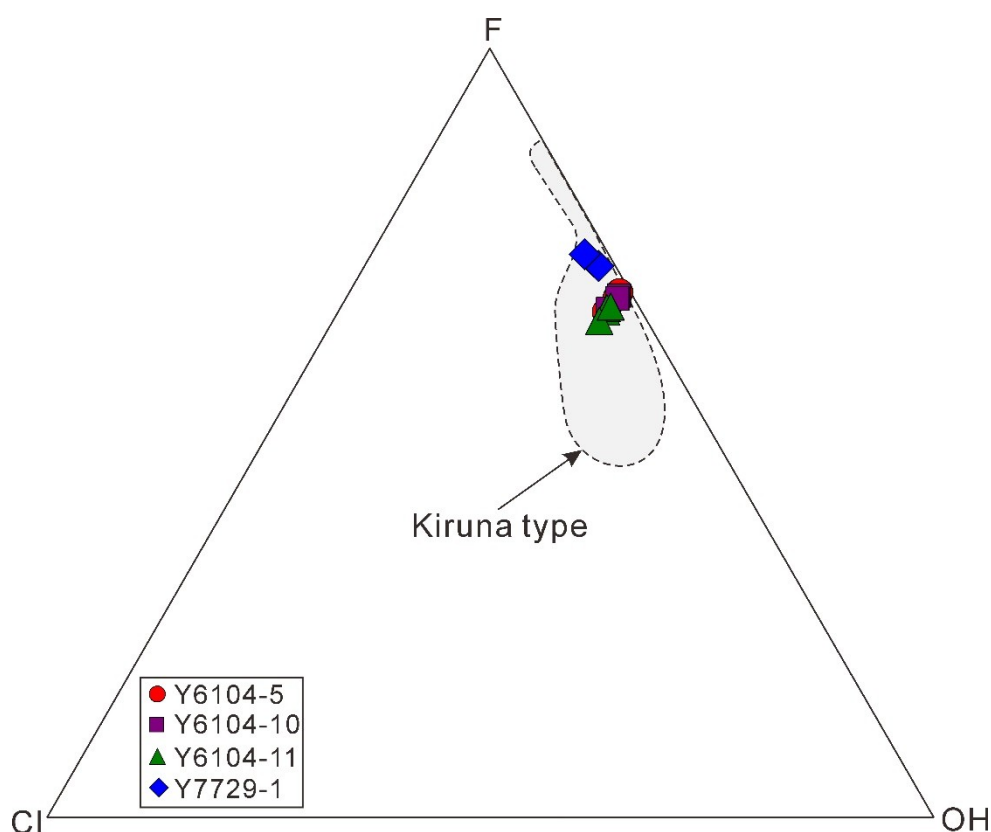


Figure 6. F-Cl-OH diagram showing compositional variation (atoms per formula unit) in apatite (modified after [29]).

5.2.2. Tourmaline

The tourmaline results of major elements analyses are shown in Table S2. Tourmaline crystals in the Yamansu deposit generally show narrow SiO_2 (33.09%–36.94%) and MgO (8.38%–10.51%) contents. According to the relationship between Fe and Mg, tourmaline crystals have low contents of FeO (5.43%–14.53%), medium–low contents of $FeO/(FeO + Mg)$ ratios, and medium–high MgO/FeO ratios (0.67–1.54), which classify Yamansu tourmaline as dravite or Mg-rich tourmaline. The calculated B_2O_3 contents of tourmaline vary between 9.39% and 10.39% (Table S2). The Al–Fe–Mg compositional ternary of tourmaline is generally used to reflect the host rock types or origin of tourmaline [30], and most of the Yamansu tourmaline crystals plot in the metapelites, metapsammites, quartz-tourmaline, and calc-silicate rocks fields (Figure 7). Moreover, as the main cations of X and Y sites in tourmaline crystals, the changes of Na and Fe sensitively reflect the relationship between tourmaline and their host rocks. The Yamansu tourmaline crystals have high contents of Na_2O (0.98%–1.80%), which is consistent with the high Na_2O contents in volcanic rocks in Yamansu ore district [31]. Normally, zoned

tourmalines are present. As shown in Figure 8, FeO, SiO₂, TiO₂, and CaO contents increase rimward, but Al₂O₃ and Na₂O contents decrease from the core to the rim, indicating a compositional change of sodium depletion and iron enrichment during the growth of tourmaline.

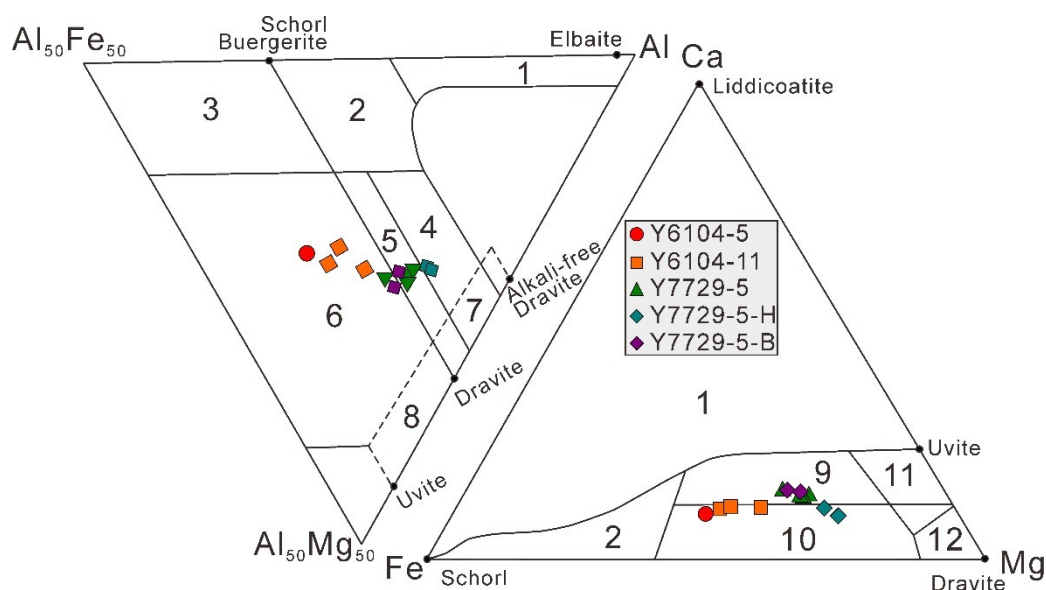


Figure 7. Compositional discrimination of tourmalines from the Yamansu deposit (modified after [30]). 1: Li-rich granitoids, pegmatites and aplites; 2: Li-poor granitoids and their associated pegmatites and aplites; 3: Fe³⁺-rich quartz-tourmaline rocks (hydrothermal altered granites); 4: Metapelites and metapsammities coexisting with Al-saturating phase; 5: Metapelites and metapsammities lacking Al-saturating phase; 6: Quartz-tourmaline rocks, calc-silicate rocks and metapelites; 7: Low-Ca meta-ultramafic rocks and metasediments; 8: Metacarbonates and metapyroxenites; 9: Ca-rich metapelites, metapsammities, and calc-silicate rocks; 10: Ca-poor metapelites, metapsammities, and quartz-tourmaline rocks; 11: Metacarbonate; 12: Metaultramafic.

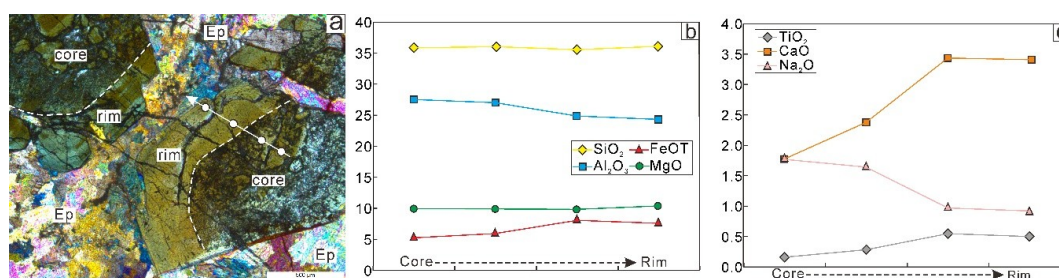


Figure 8. Major chemical element compositional profiles for the Yamansu zoned tourmaline. (a) Growth zonation and test points of tourmaline; (b,c) Variations of elements in compositional profile of tourmaline.

5.2.3. Garnet

The contents of major elements and calculated end-member compositions of garnets are listed in Table S3. Electron microprobe analyses show that garnet crystals from the Yamansu deposit belong to the andradite–grossular solid solutions with less pyrope (sum of pyrope, spessartine, almandine, and uvarovite) (Figure 9).

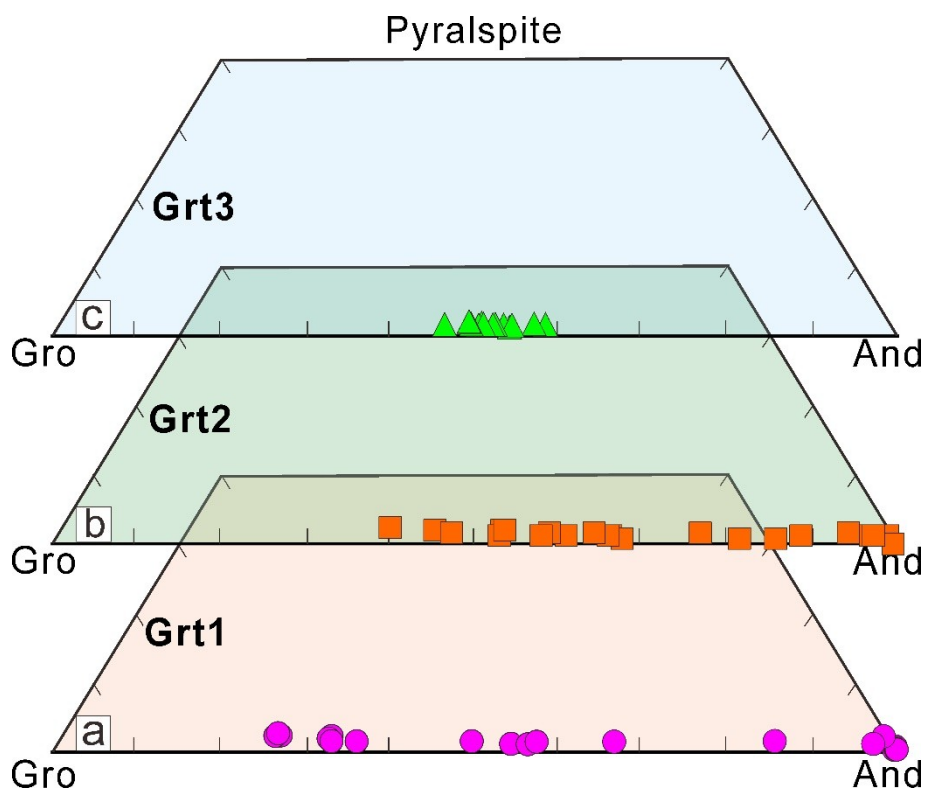


Figure 9. Triangular classification of garnets in the Yamansu deposit (the base diagram is modified after [32]). (a) Grt1—Garnets of the first generation with dramatic changes of end-member compositions (andradite and grossular); (b) Grt2—Garnets of the second generation with relative enrichment of andradite contents; (c) Grt3—Garnets of the third generation with little variation in end-member compositions. And = andradite; Gro = grossular; Pyralspite = spessartine + pyrope + almandine + uvarovite.

Grt1 have narrow compositional ranges in SiO_2 and CaO but wide compositional ranges in FeO_T and Al_2O_3 . The contents of MnO and MgO are remarkably low (less than 1%). The end-member compositions of Grt1 show dramatic changes consisting of $\text{And}_{25.33-99.88}\text{Gro}_{0.00-72.42}$ with minor $\text{Pys}_{0.12-2.40}$ (Figure 9a). Profile along the crystal zonation of Grt1 (sample Y7729-1) records compositional changes where Fe content decreases first and then increases rimward, but Al content increases first and then decreases with negligible changes in Ca and Si content in the core (Figure 10a).

Compared with Grt1, Grt2 show narrow compositional ranges in SiO_2 and CaO but have relatively higher FeO_T and lower Al_2O_3 contents. Similarly, MnO and MgO contents of Grt2 are remarkably low (less than 1.00%). The calculated end-member compositions of Grt2 also show dramatic changes consisting of $\text{And}_{38.71-99.94}\text{Gro}_{0.00-58.80}$ with minor $\text{Pys}_{0.06-2.49}$ (Figure 9b). Well-preserved chemical growth zonations and their analysis results generally show a general decrease in FeO_T or andradite contents and increase in Al_2O_3 or grossular contents from core to rim (Figure 10b,c). For the sample Y5817-5, SiO_2 and CaO contents gradually increase, and FeO_T content decreases first and then increases but Al_2O_3 content increases first and then decreases from core to rim (Figure 10b). The variations of SiO_2 and CaO contents in the sample Y5818-3 are smooth from core to rim. However, FeO_T (or andradite) and Al_2O_3 (or grossular) contents show “M” and “W” patterns in variations, respectively, from core to rim (Figure 10c). These features indicate clear indications of multi-stage growth. In general, there is a negative correlation between FeO_T and Al_2O_3 contents in Yamansu garnets.

Grt3 are characterized by little variation in SiO_2 (36.10%–37.81%) and CaO (32.65%–34.35%) contents and relatively low FeO_T (16.47%–19.75%) but high Al_2O_3 (7.61%–10.41%) contents. Grt3 have nearly equal andradite and grossular end-member compositions ($\text{And}_{45.35-57.64}\text{Gro}_{40.63-52.80}$)

(Figure 9c). Andradite decreases, whereas grossular increases from core towards outer rim in Grt3 (Figure 10d).

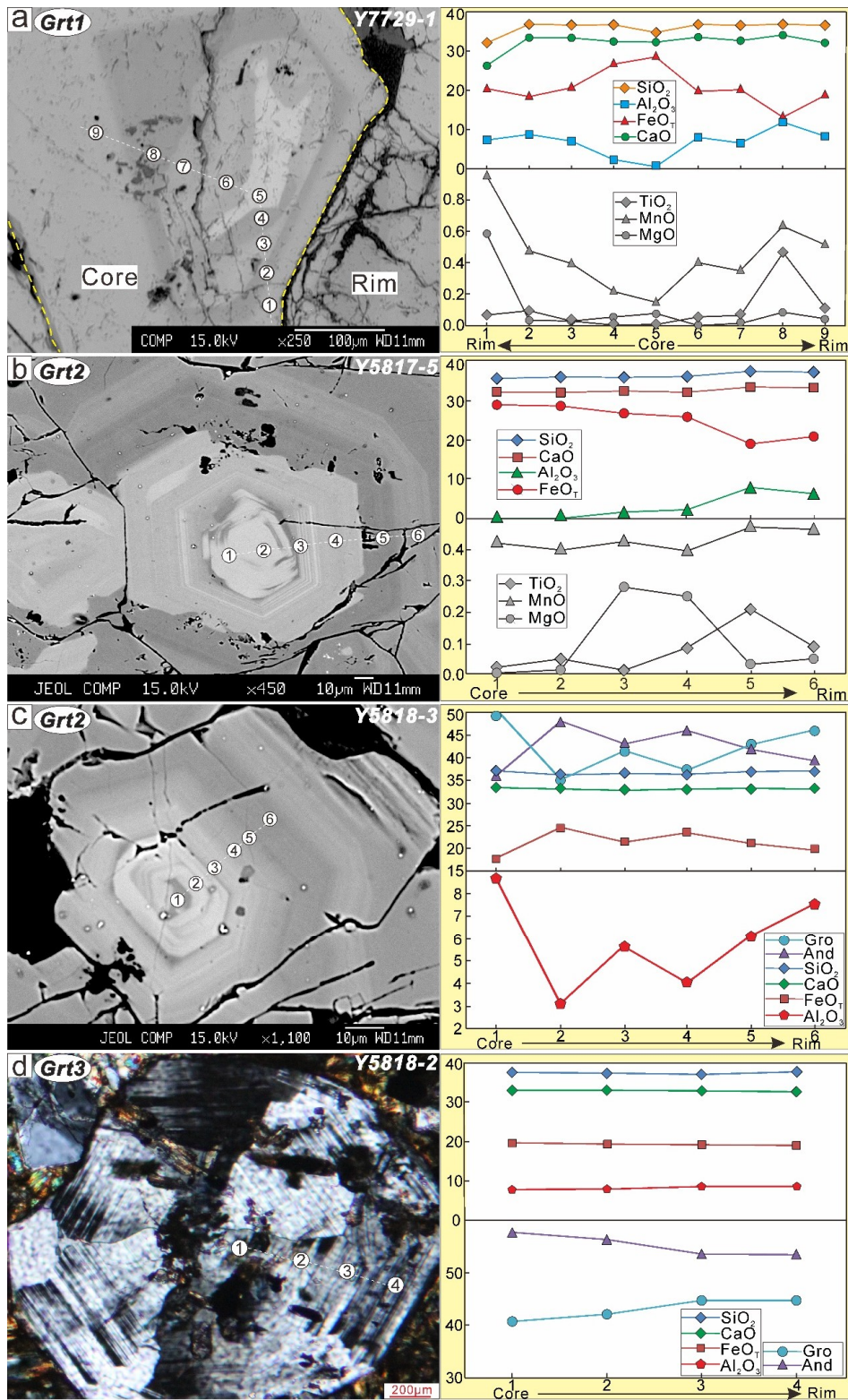


Figure 10. Back-scattered electron and cross polarized light images for different generations of garnets and their compositional profiles in the Yamansu deposit.

5.2.4. Albite and K-Feldspar

Feldspars in the Yamansu deposit can be divided into two groups: Na-plagioclase (albite) and K-feldspar. The compositions of feldspars are listed in Table S4. The SiO_2 and Al_2O_3 contents of albites vary from 67.65% to 69.73% and from 19.56% to 20.65%, respectively. Albite crystals have high Na_2O contents (11.15%–12.01%) and low CaO and K_2O (less than 1%) contents. The K-feldspar crystals contain 63.84%–64.45% of SiO_2 , 17.85%–18.10% of Al_2O_3 , and they have high K_2O (15.71–16.14%) and low CaO and Na_2O contents. Albites plot in albite field whereas K-feldspars plot in sanidine field in the Or-Ab-An triangular classification diagrams (Figure 11).

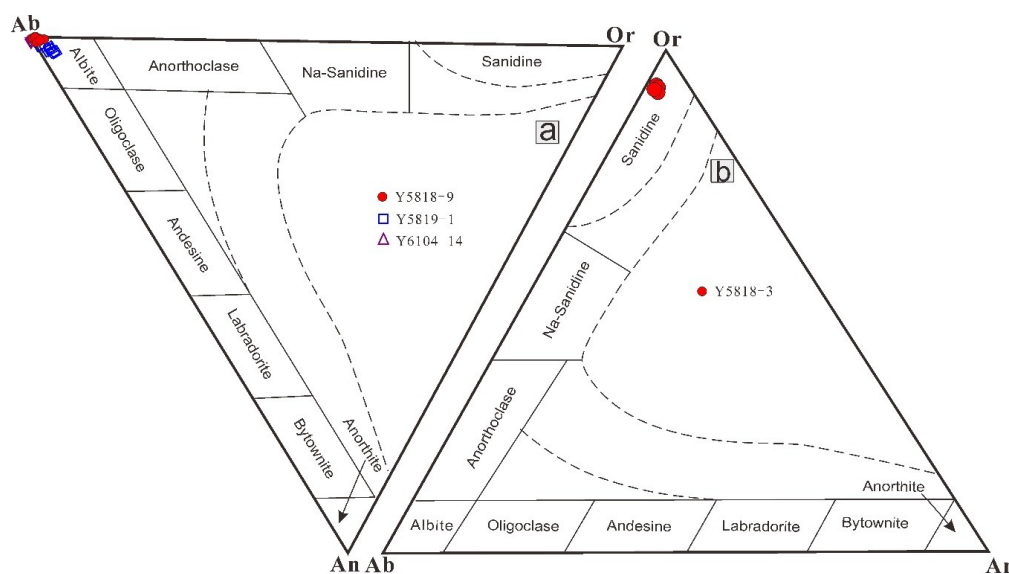


Figure 11. Albite–anorthite–orthoclase diagram (modified from [33]) for plagioclase minerals in the Yamansu deposit.

5.2.5. Axinite

The representative major element chemical compositions of axinites are shown in Table S5. The SiO_2 and CaO contents range from 42.66% to 43.84% and from 19.16 to 19.88%, respectively. The average contents of FeO and Al_2O_3 in Yamansu axinite are 7.16% and 15.79%, respectively. The calculated B_2O_3 contents vary from 6.63 to 7.02%. According to the $\text{FeO}/(\text{MnO} + \text{FeO})$ ratios (0.52–0.72) and Mg–Al–Fe triangular diagram, Yamansu axinites belong to the ferroxinite (Figure 12).

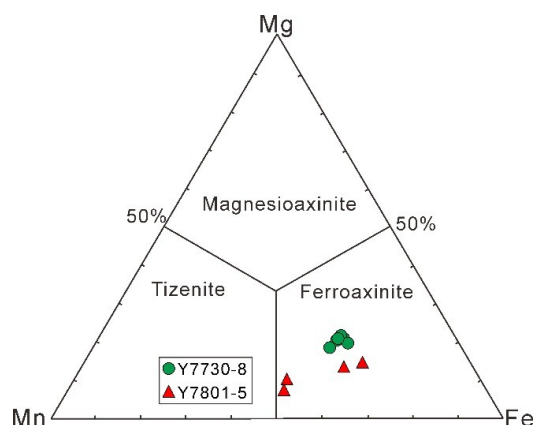


Figure 12. Chemical compositions discrimination of axinite in the Yamansu deposit (modified from [34]).

5.3. Trace Elements

The trace element analyses by LA-ICP-MS in the Yamansu deposit are based on different generations of garnets. The cores from each generation garnet were analyzed and their chemical compositions are presented in Table S6.

Grt1 have medium total rare earth element ($\Sigma\text{REE} = 24.46\text{--}39.90$ ppm) contents and high fractionations between light and heavy rare earth element ($\text{LREE}/\text{HREE} = 0.44\text{--}2.17$) with with variable Eu anomalies ($\delta\text{Eu} = 0.95\text{--}1.65$). Chondrite-normalized REE patterns of Grt1 show a steep left-leaning LREE segment and a flat HREE segment (Figure 13). Grt1 show extreme depletions of large ion lithophile elements (LILEs: sum of Rb, Sr, Cs and Ba = 0.10–5.64 ppm) and U (0.60–4.28 ppm) contents but relatively enrichments of high field strength element (HFSEs: sum of Nb, Ta, Zr, and Hf = 9.53–87.04 ppm), Y (12.95–54.98 ppm) and Ho (0.55–1.26 ppm) contents.

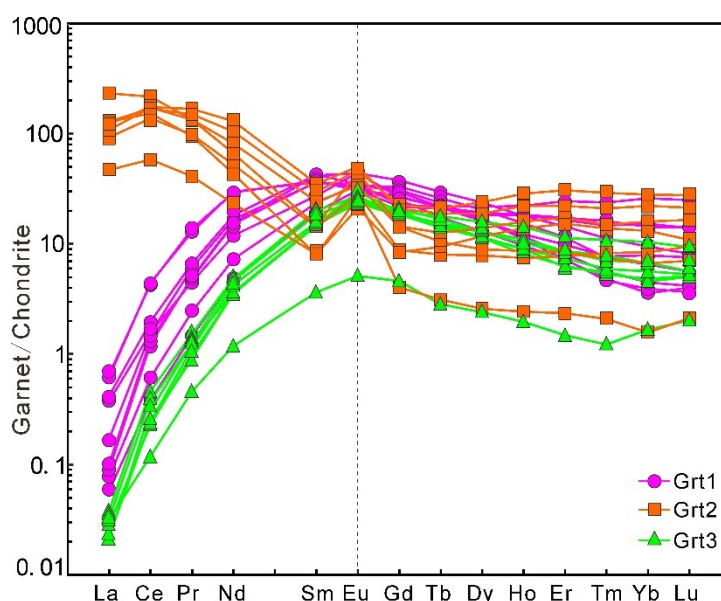


Figure 13. Chondrite-normalized rare earth element (REE) distribution patterns for three generations of garnets from the Yamansu deposit. The chondrite-normalized values were calculated by [35].

Grt2 have the highest ΣREE (75.28–250.62 ppm) contents and variable ΣLREE (64.04–236.38 ppm) and ΣHREE (2.50–24.41 ppm). They are LREE-enriched and HREE-depleted ($\text{LREE}/\text{HREE} = 5.70\text{--}62.31$ ppm) with positive Eu anomalies ($\delta\text{Eu} = 1.75\text{--}4.47$) (Figure 13). Grt2 are characterized by relatively high LILEs (0.34–5.10 ppm) and U (23.98–58.64 ppm) contents but a spread of HFSEs (4.83–111.97 ppm) and Y (4.62–68.91 ppm) contents.

Grt3 have low ΣREE (3.94–19.49 ppm) contents and show LREE-enriched and HREE-depleted ($\text{LREE}/\text{HREE} = 0.42\text{--}0.71$) patterns with weak positive Eu anomalies ($\delta\text{Eu} = 1.29\text{--}1.73$) (Figure 13). Grt3 contain low concentrations of U (0.30–1.60 ppm) and Y (2.93–19.91 ppm) but high concentrations of HFSEs (21.80–60.53 ppm).

6. Discussion

6.1. Physicochemical Conditions

6.1.1. Fluid Properties

The ore-forming fluid in a magmatic–hydrothermal system is characterized by large amounts of volatiles and dissolved metal elements [36,37]. The presence of apatite and tourmaline is well developed in Stage I, indicating that the Yamansu ore-forming fluid formed under high temperatures with considerable volatiles. The Grt1 in Stage I show variations in composition

and have grossular-rich cores without oscillatory zoning, which reflects retrograde high-temperature minerals [38]. The characteristics of the REEs from Grt1 (Figure 14a) are similar to those resulting from REE partitioning in high-temperature fluids and silicate melts (relative depletions in REEs and variable Eu anomalies), implying that the ore-forming fluid in Stage I was derived from a magmatic–hydrothermal source [39,40]. This interpretation is confirmed by melt inclusions in the garnets of the early stage [41]. In addition, abrupt compositional variations between the cores and rims (Figure 5e) indicate that Grt1 grew under rapidly changing physicochemical conditions, which are interpreted as changes in the composition-dependent fluid influx [42,43].

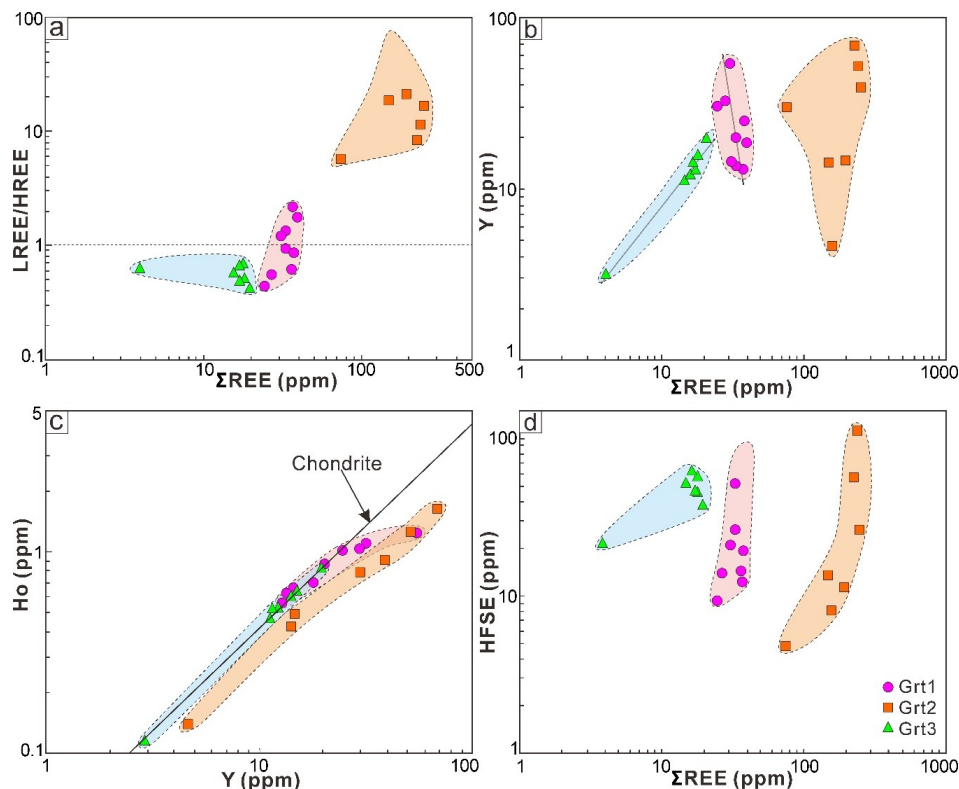


Figure 14. Binary plots of (a) total rare earth element (Σ REE) versus light and heavy rare earth element (LREE/HREE), (b) Σ REE versus Y, (c) Y versus Ho, and (d) Σ REE versus high field strength element (HFSE) for garnets from the Yamansu deposit. The chondritic Y/Ho ratio (c) is from [44].

In Stage II, the ore-forming fluid probably inherited the properties of the early fluid with a high temperature but a different fluid composition. K-feldspar is represented in this stage, and hydrothermal fluids with alkali-rich contents can promote the enrichment and migration of iron contents [45]. During the main metallogenic stage (Stage III), the occurrences of magnetite and retrograde skarn minerals, such as chlorite and epidote, reflect moderate- to high-temperature conditions for the ore-forming fluid [46]. Yttrium and REEs have similar geochemical properties and they show almost linear correlations. The Yamansu Grt2 samples, however, show insignificant correlations between REEs and Y (Figure 14b), which might reflect either local protolith chemical heterogeneities or changes in the fluid composition during Stage II [10,47]. Moreover, the fractionation of Y and Ho twin pairs from the chondritic ratio (Figure 14c) is an indication that Grt2 growth occurred in a complex hydrothermal fluid system [44,48]. This result is supported by carbon and oxygen isotope data [5].

The representative quartz + sulfides, quartz + calcite, and quartz + axinite veins that cut early-stage mineral assemblages (Figure 4h,i) signify that the ore-forming fluid in Stage IV was generated under low-temperature conditions after iron precipitation. Although Grt3 crystals are present in Stage IV, they have low Σ REE, Y, and Y/Ho contents, and high contents of HFSEs (Figure 14c,d). This disparity results from differences in the fluid composition and fluid flow rate [12].

6.1.2. Oxygen Fugacity

Studies of end-member compositions in garnets suggest that increasing oxygen fugacity (fO_2) may result in an increase in andradite content during garnet growth [42,49]. The Yamansu Grt1 cores are dominated by grossular end-member compositions, and andradite compositions increase from the Grt1 rims to the Grt2 cores (Figure 5e–h), suggesting an increase in fO_2 from Stage I to Stage II [50]. Theoretical and experimental data for variable valence elements (such as Eu, U, and Cr) in hydrothermal fluids also imply that increasing high-valence activity with increasing fO_2 during the fluid process may result in increases in the corresponding element contents [51–53]. The results showing increasing δEu and U contents from Grt1 to Grt2 (Figure 15a,b) reveal an increase in fO_2 of the fluid from Stage I to Stage II. High oxygen fugacity conditions are favorable for the deposition of iron ores. Therefore, the development of abundant magnetite, chlorite, and epidote, which formed in Stage III, can be interpreted as a gradually increase in fO_2 during the evolution of the ore-forming fluid during Stage III [54,55].

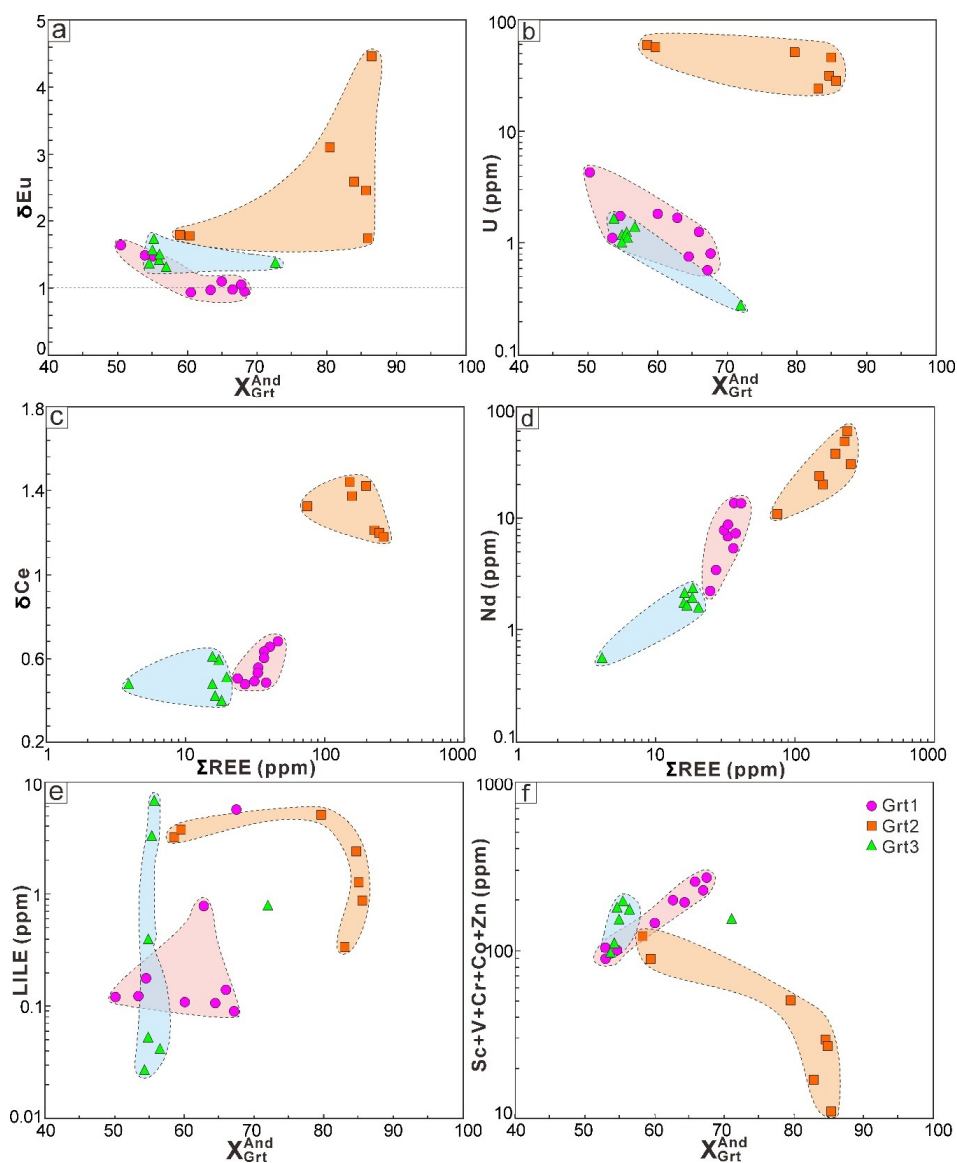


Figure 15. Binary plots of (a) proportions of andradite in garnet versus Eu anomalies (δEu), (b) proportions of andradite in garnet versus U, (c) ΣREE versus δCe , (d) ΣREE versus Nd, (e) proportions of andradite in garnet versus large ion lithophile elements (LILE), and (f) proportions of andradite in garnet versus siderophile elements (sum of Sc, V, Cr, Co, and Zn) for garnets from the Yamansu deposit.

6.1.3. pH

In addition to the fluid properties in a hydrothermal system, the temperature, cation type, and fluid density also play important roles in the pH of the fluid. Therefore, it is inappropriate to separately describe the pH based on fluid composition [56]. Fortunately, REEs and some immobile trace elements in hydrothermal fluids are scarcely affected in magmatic–hydrothermal fluids, and pH is largely correlated with their total contents in the fluid [44,57]. It was demonstrated by [52] that LREE-depleted and HREE-enriched patterns with negative or no Eu anomalies form under nearly neutral pH, whereas LREE-enriched and HREE-depleted patterns develop under mildly acidic pH, and the Eu anomalies are positive or significantly controlled by the complexing agents (mainly F, Cl and B). The Yamansu Grt1 crystals are characterized by variable LREE/HREE and δEu values (both show values >1 and <1) (Figures 14a and 15a), which may be due to the influences of the complexing agents (such as F, Cl, and P) in the early stage [7,58]. This interpretation agrees well with the presence of apatite and tourmaline in Stage I. In comparison, the Grt2 crystals show LREE-enriched and HREE-depleted patterns with positive Eu anomalies (Figure 13), suggesting that a mildly acidic pH is recorded for Stage II. This particular pH condition is favorable for the enrichment and mineralization of Fe contents in ore-forming fluids [59].

An investigation by [57] of thermal fluids found that pH strongly controls the changes in REEs and Ce anomalies and shows obvious negative correlations with ΣREE and δCe . Moreover, theoretical and thermodynamic experiments suggested that pH significantly affects the fractionation of ΣREE and Nd and that pH is negatively correlated with ΣREE and Nd in hydrothermal fluids [52,60]. An early increasing trend followed by a decreasing trend for the ΣREE , δCe , and Nd contents from Stage I to Stage IV (Figure 15c,d) indicate a decrease and then an increase in pH during the evolution of the Yamansu hydrothermal fluid.

6.2. Ore-Forming Fluid Evolution

The mineral assemblages of the Yamansu deposit and their geochemical characteristics may reflect the evolution of the hydrothermal fluid. The results for the Grt1 crystals with low ΣREE and LILEs contents but high HFSEs, Y, and Ho contents (Figures 14 and 15) indicate that the ore-forming fluid in Stage I formed under near equilibrium condition within a closed system with low W/R ratios [40,61]. During the early stage, the ore-forming fluid likely experienced diffusive metasomatism, and the fluid flow and mineral growth rates were slow [62]. From Stage II to Stage III, the fluid commonly shows major changes, namely a fluctuating composition associated with minerals ranging from garnet (oscillatory zoning, Figure 5g,h) to magnetite (oscillatory zoning, Figure 5i) and chlorite. Such dynamic and repetitive enrichments and depletions in composition require the fluid flow to have been episodic, which may have been caused by periods of metasomatism between hydrothermal fluid and wall rocks [63]. In particular, irregular Grt2 cores, which are characterized by high ΣREE , LREE/HREE, δEu , and δCe contents, and deviations of Y/Ho ratios from the chondritic linear trend (Figures 14 and 15), have been proposed to be responses to the nonequilibrium system [40,62]. This situation was mostly followed by high W/R ratios and relatively high $f\text{O}_2$ under infiltrative metasomatism with the introduction of a batch of externally derived fluid [64]. Note that the decreasing andradite (Figures 5h and 10b) indicates that the Fe content in the fluid decreased gradually and could be explained by introducing ore-forming material (Fe) into the late stage (Stage III). This evolutionary interpretation is supported by the replacement of garnets in Stage II by subsequent magnetite in Stage III (Figure 4d,e and Figure 5f,g).

6.3. Implications for Mineralization

Although skarn minerals such as garnet, chlorite, and epidote are present, skarn zones and associated intrusive rocks have not been identified in the Yamansu ore district [2], implying the absence of an obvious relationship between the formation of skarns and intrusive rocks. In addition, the presence of albite, apatite, and tourmaline coupled with the near absence of diopside in the early stage

and the multigeneration garnets, together with the chlorite and epidote skarns cut by later garnet veins (Figure 4h,i), indicate that Yamansu differs from typical contact metasomatic skarn-type deposits. Previous studies on the field geology and geochronology of the diagenesis and mineralization of this deposit attributed the Yamansu mineralization to volcanic rocks [1–3,5]. As discussed above, the geochemistry of tourmaline has a homologous relationship with volcanic rocks; additionally, the ore-forming fluid formed under high temperatures with considerable volatiles in Stage I. Therefore, the Yamansu ore-forming fluid was likely derived from a volcanic magmatic–hydrothermal fluid.

Studies have suggested that metallogenic materials in fluids are transported mainly as complex compounds in most hydrothermal deposits [65,66]. Volatile elements (such as B and Cl) and alkaline elements (such as Na and K) easily form complex compounds, and these complex compounds may have transported considerable metallogenic materials in the early stage of the Yamansu deposit. This hypothesis is supported by the Cl-rich fluid in the early stage of Yamansu mineralization [67]. The Grt1 crystals have the highest contents of siderophile elements (Sc, V, Cr, Co, and Zn) (Figure 15f), indicating that these elements were enriched in the fluid from the early stage. The preserved concentration of Fe in the early stage fluid was low, as recorded by the Grt1 cores and tourmaline cores (Figure 16a); therefore, reaching saturation of the Fe concentration for precipitation was difficult. Furthermore, the temperature did not significantly decrease in Stage I, which hindered the precipitation of ore minerals [67]. From Stage I to Stage II, mineral geochemistry shows that the Fe content increased gradually (Figure 16b), implying that ore-forming materials accumulated within the ore-forming fluid. The Yamansu ore-forming fluid experienced changing physicochemical conditions, namely, from reducing conditions with neutral pH to oxidizing conditions with mildly acidic pH from Stage I to Stage II (Figure 16a,b). These changes were favorable for the transport and accumulation of ore-forming materials. During the migration of an ore-forming fluid, mineral precipitation occurs when fluid properties or physicochemical conditions change with time. Thus, the permeability may eventually be reduced, obstructing fluid channels [68]. Then, a strong pressure increase could have caused hydraulic fracturing when the hydrostatic pressure exceeded the lithostatic pressure. It follows, then, that breccia magnetite ores were present (Figure 4d). However, the permeability increased as a result of the opening of fractures and a decrease in pressure, which in turn promoted mineral formation. Ultimately, the fluid system was created and destroyed periodically (Figure 16c); and consequently, the magnetite composition may have been controlled by dissolution-reprecipitation processes under fluctuating physicochemical conditions [69,70]. Therefore, massive ores containing magnetite exhibiting oscillatory zoning were deposited under these fluctuating conditions during Stage III (Figure 5i). Nevertheless, Grt3 formed in Stage IV due to the depletion of ore-forming materials (Fe) in the fluid and the presence of unfavorable physicochemical conditions (such as low fO_2 and low W/R ratios) (Figure 16d) for the precipitation of iron; but quartz, sulfides, axinite, and calcite precipitated in the late stage.

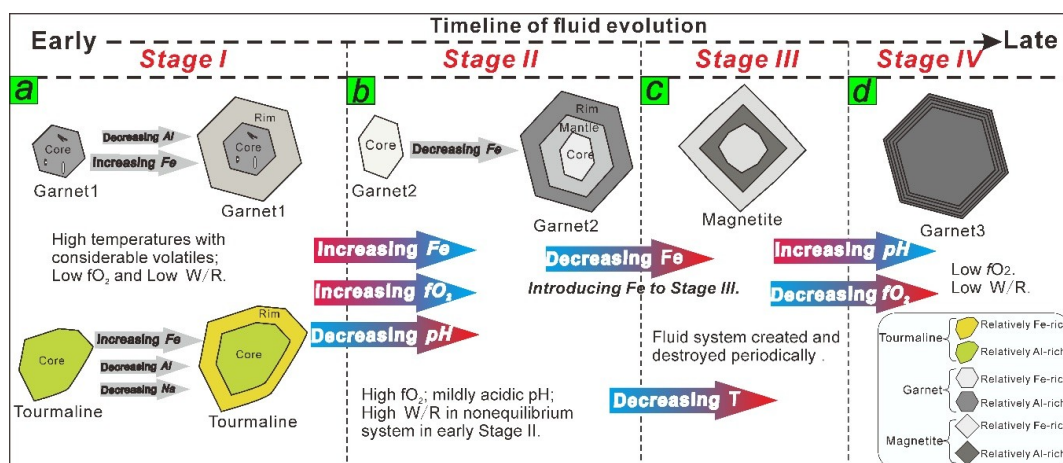


Figure 16. Schematic timeline of fluid evolution model for the Yamansu deposit. (a) Ore-forming fluid in Stage I was characterized by high temperatures with considerable volatiles, low fO_2 and low W/R ratios. Ore-forming fluid showed increasing Fe contents in the early stage; (b) The Fe content in the ore-forming fluid increased from Stage I to Stage II. The physicochemical conditions were characterized by high fO_2 , mildly acidic pH, and high W/R ratios in Stage II. The decreased Fe contents were favorable for accumulation of ore-forming materials in Stage II; (c) The decreasing temperature, periodical changes of fluid system, and fluctuating physicochemical conditions caused the deposition of oscillatory zoning magnetite in Stage III; (d) Ore-forming fluid in Stage IV was characterized by depletion of ore-forming materials (Fe contents), low fO_2 , and low W/R ratios.

7. Conclusions

Four alteration and mineralization stages are distinguished in the Yamansu deposit based on the field geology, petrographic observations, and mineral geochemistry studies. The ore-forming fluid was derived from a magmatic–hydrothermal source and contained considerable volatiles and metallogenic materials in the early stage but experienced different physicochemical conditions in the subsequent stages. The magnetite ores of the major mineralization stage were deposited in a fluctuating fluid system. Multistage fluctuations of the hydrothermal fluid may have been the main mechanism for the enrichment and precipitation of metallogenic materials.

Supplementary Materials: The following are available online at <http://www.mdpi.com/2075-163X/10/1/39/s1>, Table S1: EMPA data of the apatite in the Yamansu deposit, Table S2: EMPA data of the tourmaline in the Yamansu deposit, Table S3: EMPA data of the different generations of garnet in the Yamansu deposit, Table S4: EMPA data of the plagioclase and K-feldspar in the Yamansu deposit, Table S5: EMPA data of the axinite in the Yamansu deposit, Table S6: LA-ICP-MS trace element (ppm) compositions of different generations of garnets in the Yamansu deposit.

Author Contributions: J.W., Y.W., and L.L. offered advice to this work; Z.S., Y.W., and L.L. finished the field work; Z.S. performed the experiments and organized this paper. All authors have read and agreed to the published version of the manuscript.

Funding: This research was funded by the National Key R&D Program of China (2018YFC0604006, 2017YFC0601204) and the National Basic Research Program of China (973 Program, No. 2014CB440803).

Acknowledgments: We would like to thank Di Zhang and Qian Mao with the Institute of Geology and Geophysics, Chinese Academy of Sciences, for providing technical support in the microprobe analyses. We would like to thank Dengfeng Li and Ying Liu from the Key Laboratory of Marine Resources and Coastal Engineering, Sun Yat-sen University, for the trace element analyses of the garnets by LA-ICP-MS. Additionally, many reviewers have provided numerous comments, which helped significantly improve the clarity and quality of this manuscript.

Conflicts of Interest: The authors declare no conflict of interest.

References

1. Hou, T.; Zhang, Z.C.; Santosh, M.; Zhu, J.; Luo, W.J. Geochronology and geochemistry of submarine volcanic rocks in the Yamansu iron deposit, Eastern Tianshan Mountains, NW China: Constraints on the metallogenesis. *Ore Geol. Rev.* **2014**, *56*, 487–502. [[CrossRef](#)]
2. Li, H.M.; Ding, J.H.; Li, L.X.; Yao, T. The genesis of the skarn and the genetic type of the Yamansu iron deposit, Eastern Tianshan, Xinjiang. *Acta Geol. Sin.* **2014**, *88*, 2477–2489, (In Chinese with English abstract).
3. Li, H.M.; Ding, J.H.; Zhang, Z.C.; Li, L.X.; Chen, J.; Yao, T. Iron-rich fragments in the Yamansu iron deposit, Xinjiang, NW China: Constraints on metallogenesis. *J. Asian Earth Sci.* **2015**, *13*, 1068–1081. [[CrossRef](#)]
4. Li, W.M.; Chen, G.Y.; Sun, S.R. A study on the mineral paragenesis of Yamansu iron deposit. *Explor. Nat.* **1986**, *5*, 119–125, (In Chinese with English abstract).
5. Huang, X.W.; Zhou, M.F.; Beaudoin, G.; Gao, J.F.; Qi, L.; Lyu, C. Origin of the volcanic-hosted Yamansu Fe deposit, Eastern Tianshan, NW China: Constraints from pyrite Re-Os isotopes, stable isotopes, and in situ magnetite trace elements. *Ore Geol. Rev.* **2018**, *53*, 1039–1060. [[CrossRef](#)]
6. Yardley, B.W.D.; Rochelle, C.A.; Barnicoat, A.C.; Lloyd, G.E. Oscillatory zoning in metamorphic minerals: An indicator of infiltration metasomatism. *Mineral. Mag.* **1991**, *55*, 357–365. [[CrossRef](#)]
7. Jamtveit, B. On the origin of zoned grossular-andradite garnets in hydrothermal systems. *Eur. J. Mineral.* **1995**, *7*, 1399–1410. [[CrossRef](#)]
8. Konrad-Schmolke, M.; O'Brien, P.J.; Capitani, C.D.; Carswell, D.A. Garnet growth at high- and ultra-high pressure conditions and the effect of element fractionation on mineral modes and composition. *Lithos* **2008**, *103*, 309–332. [[CrossRef](#)]
9. Ding, T.; Ma, D.S.; Lu, J.J.; Zhang, R.Q. Garnet and scheelite as indicators of multi-stage tungsten mineralization in the Huangshaping deposit, southern Hunan province, China. *Ore Geol. Rev.* **2018**, *94*, 193–211. [[CrossRef](#)]
10. Gaspar, M.; Meinert, L.D.; Moretti, R. REE in skarn systems: A LA-ICP-MS study of garnets from the Crown Jewel gold deposit. *Geochim. Cosmochim. Acta* **2008**, *72*, 185–205. [[CrossRef](#)]
11. Zhai, D.G.; Liu, J.J.; Zhang, H.Y.; Wang, J.P.; Su, L.; Yang, X.A.; Wu, S.H. Origin of oscillatory zoned garnets from the Xieertala Fe–Zn skarn deposit, northern China: In situ LA-ICP-MS evidence. *Lithos* **2014**, *190*, 279–291. [[CrossRef](#)]
12. Baghban, S.; Hosseinzadeh, M.; Moayyed, M.; Mokhtari, A.A.; Gregory, D.D. Geology, mineral chemistry and formation conditions of calc-silicate minerals of Astamal Fe-LREE distal skarn deposit, Eastern Azarbaijan province, NW Iran. *Ore Geol. Rev.* **2015**, *68*, 79–96. [[CrossRef](#)]
13. Windley, B.F.; Alexeiev, D.; Xiao, W.J.; Kröner, A.; Badarch, G. Tectonic models for accretion of the Central Asian Orogenic belt. *J. Geol. Soc.* **2007**, *164*, 31–47. [[CrossRef](#)]
14. Xiao, W.J.; Windley, B.F.; Allen, M.B.; Han, C.M. Paleozoic multiple accretionary and collisional tectonics of the Chinese Tianshan orogenic collage. *Gondwana Res.* **2013**, *23*, 1316–1341. [[CrossRef](#)]
15. Chen, H.Y.; Wan, B.; Franco, P.; Chen, Y.J.; Xiao, B. Metallogenesis of the Xinjiang Orogens, NW China—New discoveries and ore genesis. *Ore Geol. Rev.* **2018**, *100*, 1–11. [[CrossRef](#)]
16. Wang, J.B.; Wang, Y.W.; He, Z.J. Ore deposits as a guide to the tectonic evolution in the East Tianshan Mountains, NW China. *Geol. China* **2006**, *33*, 461–469, (In Chinese with English abstract).
17. Deng, X.H.; Wang, J.B.; Pirajno, F.; Wang, Y.W.; Li, Y.C.; Li, C.; Zhou, L.M.; Chen, Y.J. Re-Os dating of chalcopyrite from selected mineral deposits in the Kalatag district in the eastern Tianshan orogen, China. *Ore Geol. Rev.* **2016**, *77*, 72–81. [[CrossRef](#)]
18. Mao, J.W.; Goldfarb, R.J.; Wang, Y.T.; Hart, C.T.; Wang, Z.L.; Yang, J.M. Late paleozoic base and precious metal deposits, East Tianshan, Xinjiang, China: Characteristics and geodynamic setting. *Episodes* **2005**, *28*, 23–30. [[CrossRef](#)]
19. Zhang, Z.C.; Chai, F.M.; Xie, Q.H. High-angle subduction in a thermal structure with warm mantle-cool crust: Formation of submarine volcanics-hosted iron deposits. *Geol. China* **2016**, *43*, 367–379, (In Chinese with English abstract).
20. Dong, L.H.; Feng, J.; Zhuang, D.Z.; Li, F.M.; Qu, X.; Liu, D.Q.; Tang, Y.L. Discussion of metallogenic models, mineralization characteristic and main type of rich-iron ore of Xinjiang. *Xinjiang Geol.* **2011**, *29*, 416–422, (In Chinese with English abstract).

21. Qin, K.Z.; Zhang, L.C.; Xiao, W.J. Overview of major Au, Cu, Ni and Fe deposits and metallogenic evolution of the eastern Tianshan Mountains, Northwestern China. In *Tectonic Evolution and Metallogeny of the Chinese Altay and Tianshan*; Mao, J.-W., Goldfarb, S., Eds.; Springer: London, UK, 2003; pp. 227–249.
22. Velasco, F.; Tornos, F.; Hanchar, J.M. Immiscible iron- and silica-rich melts and magnetite geochemistry at the El Laco volcano (northern Chile): Evidence for a magmatic origin for the magnetite deposits. *Ore Geol. Rev.* **2016**, *79*, 346–366. [[CrossRef](#)]
23. Yao, P.H.; Wang, K.N.; Du, C.L.; Lin, Z.T.; Song, X. *Records of China's Iron Ore Deposits*; Metallurgical Industry: Beijing, China, 1993; pp. 1–662. (In Chinese)
24. Wang, X.B. Analysis of the geology and genesis of Yamansu Fe deposit. *Contrib. Geol. Miner. Resour. Res.* **2005**, *20*, 125–128, (In Chinese with English abstract).
25. Li, G.R.; Wu, C.Z.; Branquet, Y. Comment on “Geochronology and geochemistry of submarine volcanic rocks in the Yamansu iron deposit, Eastern Tianshan Mountains, NW China: Constraints on the metallogenesis” by Tong Hou, Zhaochong Zhang, M.; Santosh, John Encarnacion, Jiang Zhu, Wenjuan Luo [ore geology review, 56(2014): 487–502]. *Ore Geol. Rev.* **2014**, *63*, 343–345.
26. Deer, W.A.; Howie, R.A.; Zussman, J. *An Introduction to the Rock-Forming Minerals*, 2nd ed.; Mineralogical Society of Great Britain and Ireland: Twickenham, UK, 1992; p. 696.
27. Liu, Y.S.; Hu, Z.C.; Gao, S.; Gunther, D.; Xu, J.; Gao, C.G.; Chen, H.H. In situ analysis of major and trace elements of anhydrous minerals by LA-ICP-MS without applying an internal standard. *Chem. Geol.* **2008**, *257*, 34–43. [[CrossRef](#)]
28. Belousova, E.A.; Walters, S.; Griffin, W.L.; O'Reilly, S.Y. Trace element signatures of apatites in granitoids from the Mt. Isa Inlier, Northwestern Queensland. *Aust. J. Earth Sci.* **2001**, *48*, 603–619. [[CrossRef](#)]
29. Edfelt, Å.; Armstrong, R.N.; Smith, M.; mMartinsson, O. Alteration paragenesis and mineral chemistry of the Tjärrojäkka apatite–iron and Cu (–Au) occurrences, Kiruna area, northern Sweden. *Miner. Depos.* **2005**, *40*, 409–434. [[CrossRef](#)]
30. Henry, D.J.; Guidotti, C.V. Tourmaline as a petrogenetic indicator mineral: An example from the staurolite-grade metapelices of NW Maine. *Am. Mineral.* **1985**, *70*, 1–15.
31. Sun, Z.Y.; Wang, J.B.; Wang, Y.W.; Long, L.L.; Luo, Z.H.; Deng, X.H.; Hu, Q.T.; Wang, M.L. Sodium-rich volcanic rocks and their relationships with iron deposits in the Aqishan–Yamansu belt of Eastern Tianshan, NW China. *Geosci. Front.* **2019**, *7*, 27. [[CrossRef](#)]
32. Meinert, L.D. Skarns and skarn deposits. *Geosci. Can.* **1992**, *19*, 145–162.
33. Dana, J.D.; Klein, C.; Hurlbut, C.S. *Manual of Mineralogy*; Wiley: Hoboken, NJ, USA, 1993.
34. Filip, J.; Dachs, E.; Tucek, J.; Novak, M.; Bezducka, P. Low-temperature calorimetric and magnetic data for natural end-members of the axinite group. *Am. Mineral.* **2008**, *93*, 548–557. [[CrossRef](#)]
35. Sun, S.S.; McDonough, W.F. Chemical and isotopic systematic of oceanic basalts: Implications for mantle composition and processes. *Geol. Soc. Lond. Spec. Publ.* **1989**, *42*, 313–345. [[CrossRef](#)]
36. Cline, J.S.; Bodnar, R.J. Can economic porphyry copper mineralization be generated by a typical calc-alkaline melt? *J. Geophys. Res.* **1991**, *96*, 8113–8126. [[CrossRef](#)]
37. Roedder, E. Fluid inclusion evidence for immiscibility in magmatic differentiation. *Geochim. Cosmochim. Acta* **1992**, *56*, 5–20. [[CrossRef](#)]
38. Dietvorst, E.J.L. Retrograde garnet zoning at low pressure in metapeletic rocks from kemio, SW Finland. *Contrib. Mineral. Petrol.* **1982**, *79*, 37–45. [[CrossRef](#)]
39. Flynn, R.T.; Burnham, C.W. An experimental determination of rare earth partition coefficients between a chloride containing vapor phase and silicate melts. *Geochim. Cosmochim. Acta* **1978**, *42*, 685–701. [[CrossRef](#)]
40. Park, C.P.; Song, Y.G.; Kang, I.M.; Shim, J.; Chung, D.H.; Park, C.S. Metasomatic changes during periodic fluid flux recorded in grandite garnet from the Weondong W-skarn deposit, South Korea. *Chem. Geol.* **2017**, *451*, 135–153. [[CrossRef](#)]
41. Zhao, J.S.; Zhao, B.; Li, J.W.; Xu, D.R.; He, M.C.; Zheng, J.P. Magma control of magmatic skarn to the formation of some deposits of skarn type: Evidence from Laser Raman analyses of inclusions in minerals. *Acta Petrol. Sin.* **2015**, *31*, 1079–1088, (In Chinese with English abstract).
42. Jamtveit, B.; Wogelius, R.A.; Fraser, D.G. Zonation patterns of skarn garnets: Records of hydrothermal system evolution. *Geology* **1993**, *21*, 113–116. [[CrossRef](#)]
43. Jamtveit, B.; Hervig, R.L. Constraints on transport and kinetics in hydrothermal systems from zoned garnet crystals. *Science* **1994**, *263*, 505–508. [[CrossRef](#)]

44. Bau, M. Controls on the fractionation of isovalent trace elements in magmatic and aqueous systems: Evidence from Y/Ho, Zr/Hf, and lanthanide tetrad effect. *Contrib. Mineral. Petrol.* **1996**, *123*, 323–333. [[CrossRef](#)]
45. Weng, S.J.; Kong, Q.S. Mesozoic tectonism and magmatism of the lower Yangtze valley. *Bull. Chin. Acad. Geol. Sci.* **1981**, *3*, 1–20, (In Chinese with English abstract).
46. Baker, T.; Van Ryan, A.E.C.; Lang, J.R. Composition and evolution of ore fluids in a magmatic-hydrothermal skarn deposit. *Geology* **2004**, *32*, 117–120. [[CrossRef](#)]
47. Wood, S.A. The geochemistry of rare earth elements and yttrium in geothermal waters. *Spec. Publ. Soc. Econ. Geol.* **2003**, *10*, 133–158.
48. Anders, M.; Grevesse, N. Abundances of the elements: Meteoritic and solar. *Geochim. Cosmochim. Acta* **1989**, *53*, 197–214. [[CrossRef](#)]
49. Crowe, D.E.; Riciputi, L.R.; Bezenek, S.; Ignatiev, A. Oxygen isotope and trace element zoning in hydrothermal garnets: Windows into large-scale fluid-flow behavior. *Geology* **2001**, *29*, 479–482. [[CrossRef](#)]
50. Einaudi, M.T.; Meinert, L.D.; Nwberry, R.J. Skarn deposits. In *Economic Geology, 75th Anniversary*; Society of Economic Geologists: Littleton, CO, USA, 1981; Volume 1981, pp. 317–391.
51. Sverjensky, D.M. Europium redox equilibria in aqueous solution. *Earth Planet. Sci. Lett.* **1984**, *67*, 70–78. [[CrossRef](#)]
52. Bau, M. Rare-earth element mobility during hydrothermal and metamorphic fluid–rock interaction and the significance of the oxidation state of europium. *Chem. Geol.* **1991**, *93*, 219–230. [[CrossRef](#)]
53. Van Westernen, W.; Allan, N.L.; Blundy, J.D.; Purton, J.A.; Wood, B.J. Atomistic simulation of trace element incorporation into garnets—comparison with experimental garnet–melt partition data. *Geochim. Cosmochim. Acta* **2000**, *64*, 1629–1639. [[CrossRef](#)]
54. Uchida, E. Grunerite from the Shinyama ore deposit, Kamaishi mine, Japan. *Can. Mineral.* **1983**, *21*, 517–528.
55. Zhang, Z.C.; Hou, T.; Li, H.M.; Li, J.W.; Zhang, Z.H.; Song, X.Y. Enrichment mechanism of iron in magmatic-hydrothermal system. *Acta Petrol. Sin.* **2014**, *30*, 1189–1204, (In Chinese with English abstract).
56. Dziggel, A.; Wulff, K.; Kolb, J.; Meyer, F.M.; Lahaye, Y. Significance of oscillatory and bell-shaped growth zoning in hydrothermal garnet: Evidence from the Navachab gold deposit, Namibia. *Chem. Geol.* **2009**, *262*, 262–276. [[CrossRef](#)]
57. Inguaggiato, C.; Censi, P.; Zuddas, P.; Londoño, J.M.; Chacón, Z.; Alzate, D.; Brusca, L.; D’Alessandro, W. Geochemistry of REE, Zr and Hf in a wide range of pH and water composition: The Nevado del Ruiz volcano-hydrothermal system (Colombia). *Chem. Geol.* **2015**, *417*, 125–133. [[CrossRef](#)]
58. Lottermoser, B.G. Rare earth elements and hydrothermal ore formation processes. *Ore Geol. Rev.* **1992**, *7*, 25–41. [[CrossRef](#)]
59. Liang, X.J. Garnets of grossular-andradite series: Their characteristics and metasomatic mechanism. *Acta Petrol. Mineral.* **1994**, *13*, 342–352, (In Chinese with English abstract).
60. Michard, A. Rare earth element systematics in hydrothermal fluids. *Geochim. Cosmochim. Acta* **1989**, *53*, 745–750. [[CrossRef](#)]
61. Peng, H.J.; Zhang, C.Q.; Mao, J.W.; Santosh, M.; Zhou, Y.M.; Houe, L. Garnets in porphyry–skarn systems: A LA-ICP-MS, fluid inclusion, and stable isotope study of garnets from the Hongniu–Hongshan copper deposit, Zhongdian area, NW Yunnan Province, China. *J. Asian Earth Sci.* **2015**, *103*, 229–251. [[CrossRef](#)]
62. Xiao, X.; Zhou, T.F.; White, N.C.; Zhang, L.J.; Fan, Y.; Wang, F.Y.; Chen, X.F. The formation and trace elements of garnet in the skarn zone from the Xinqiao Cu-S-Fe-Au deposit, Tongling ore district, Anhui province, Eastern China. *Lithos* **2018**, *302*, 467–479. [[CrossRef](#)]
63. Jamtveit, B.; Andersen, T. Contact metamorphism of layered shale-carbonate sequences in the Oslo rift: III. The nature of skarn-forming fluids. *Econ. Geol.* **1993**, *88*, 1830–1849. [[CrossRef](#)]
64. Smith, M.P.; Henderson, P.; Jeffries, T.E.R.; Long, J.; Williams, C.T. The rare earth elements and uranium in garnets from the Beinn an Dubhaich Aureole, Skye, Scotland, UK: Constraints on processes in a dynamic hydrothermal system. *J. Petrol.* **2004**, *45*, 457–484. [[CrossRef](#)]
65. Roedder, E. Fluid inclusions. *Mineral. Soc. Am. Rev. Mineral.* **1984**, *12*, 1–644.
66. Haas, J.R.; Shock, E.L.; Sassani, D.C. Rare earth elements in hydrothermal systems: Estimates of standard partial molal thermodynamic properties of aqueous complexes of the rare earth elements at high pressures and temperatures. *Geochim. Cosmochim. Acta* **1995**, *59*, 4329–4350. [[CrossRef](#)]
67. Zeng, H. *Skarn and Ore Genesis Studying in Yamansu Iron Deposit, Eastern TianShan, Xinjiang*; Xinjiang University: Urumqi, China, 2015; pp. 1–61. (In Chinese)

68. Kolb, J. The role of fluids in partitioning brittle deformation and ductile creep in auriferous shear zones between 500 and 700 °C. *Tectonophysics* **2008**, *446*, 1–15. [[CrossRef](#)]
69. Hu, H.; Li, J.W.; Lentz, D.; Ren, Z.; Zhao, X.F.; Deng, X.D.; Hall, D. Dissolution -reprecipitation process of magnetite from the Chengchao iron deposit: Insights into ore genesis and implication for in-situ chemical analysis of magnetite. *Ore Geol. Rev.* **2014**, *57*, 393–405. [[CrossRef](#)]
70. Dare, S.A.S.; Barnes, S.J.; Beaudoin, G. Did the massive magnetite “lava flows” of El Laco (Chile) form by magmatic or hydrothermal processes? New constraints from magnetite composition by LA-ICP-MS. *Miner. Depos.* **2015**, *49*, 785–796. [[CrossRef](#)]



© 2019 by the authors. Licensee MDPI, Basel, Switzerland. This article is an open access article distributed under the terms and conditions of the Creative Commons Attribution (CC BY) license (<http://creativecommons.org/licenses/by/4.0/>).